Implementation of the FDTD method in cylindrical coordinates for dispersive materials: Modal study of C-shaped nano-waveguides

Zahia kebci [a,b], Abderrahmane Belkhir [b], Abdelaziz Mezeghrane [b], Omar Lamrous [b], Fadi Issam Baida [a,*]

[a] Département d'Optique P.M. Duffieux, Institut FEMTO-ST UMR 6174 CNRS, Université Bourgogne Franche-Comté, F-25030 Besançon, Cedex, France
[b] Laboratoire de Physique et Chimie Quantique, Faculté des Sciences, Université Mouloud MAMMERI, BP 17 RP, 15000 Tizi-Ouzou, Algeria

ARTICLE INFO

ABSTRACT

The objective of this work is to develop a code based on the finite difference time domain method in cylindrical coordinates (CC-FDTD) that integrates the Drude Critical Points model (DCP) and to apply it in the study of a metallic C-shaped waveguide (CSWG). The integrated dispersion model allows an accurate description of noble metals in the optical range and working in cylindrical coordinates is necessary to bypass the staircase effect induced by a Cartesian mesh especially in the case of curved geometrical forms. The CC-FDTD code developed as a part of this work is more general than the Body-Of-Revolution-FDTD algorithm that can only handle structures exhibiting a complete cylindrical symmetry. A N-order CC-FDTD code is then derived and used to perform a parametric study of an infinitely-long CSWG for nano-optic applications. Propagation losses and dispersion diagrams are given for different geometrical parameters.

1. Introduction

Today, the race to miniaturize optical components requires the design of new and more complex structures requiring more elaborate simulation and manufacturing tools. For this, modeling and simulation tools in nano-photonics remain a challenging field of research. They are needed to explain complex physical phenomena and to optimize the geometrical and physical parameters of a given optical component in addition to its experimental design often very expensive. One of the useful methods in this field is the finite difference time domain (FDTD) [1,2]. This method, generally developed in Cartesian coordinates and based on the Yee scheme [2,3], can be implemented in cylindrical coordinates to accurately describe structures having a curved geometry. The modeling of these structures by classical Cartesian FDTD requires a very fine spatial discretization leading to a huge computation time together with a large memory space. In the case of revolution symmetrical structures, the azimuthal angle dependence of the electromagnetic field can be developed analytically in Fourier series. This leads to the well-known BOR-FDTD (Body Of Revolution-FDTD) algorithm where no discretization along the azimuthal angle is required [1,4].

In this work we extend the BOR-FDTD code to the case of structures having a partial cylindrical symmetry. For this purpose, a CC-FDTD (Cylindrical Coordinates-FDTD) algorithm [5–8] is developed for dispersive materials where the azimuthal angle derivative appearing in Maxwell's equations is discretized through a centered finite difference scheme as for the two other coordinates (radial and axial coordinates). Compared to the BOR-FDTD algorithm, the CC-FDTD addresses the case of any polarization state while one numerical simulation per azimuthal mode number (m with a field dependence $\exp(im\phi)$) is required within the BOR-FDTD. In addition, we incorporate the Drude critical points model (DCP) [9–11] that allows a very good description of the dispersion properties of noble metals over a large spectral range in view of modeling propagation inside metallic nano-waveguides.

An order-N FDTD code [4,12,13] is then derived in cylindrical coordinates to study the propagation properties of infinitely-long waveguides. The principle of the order-N algorithm is very simple and consists on exciting the structure by an initial field that verifies Maxwell's equations in addition to exhibit a broad spectrum covering all the possible eigenfrequencies of the structure. Then the code processes the field variations versus time. After the transient regime, only the eigenmodes of the structure remain and can be determined by calculating the spectral energy density $W(\lambda) = \frac{1}{2}(\vec{E}.\vec{D} + \vec{B}.\vec{H})$. To validate our code, several tests and convergence studies are achieved by comparing with other numerical simulations (BOR and Cartesian FDTD). After that, we applied this

---

* Corresponding author.
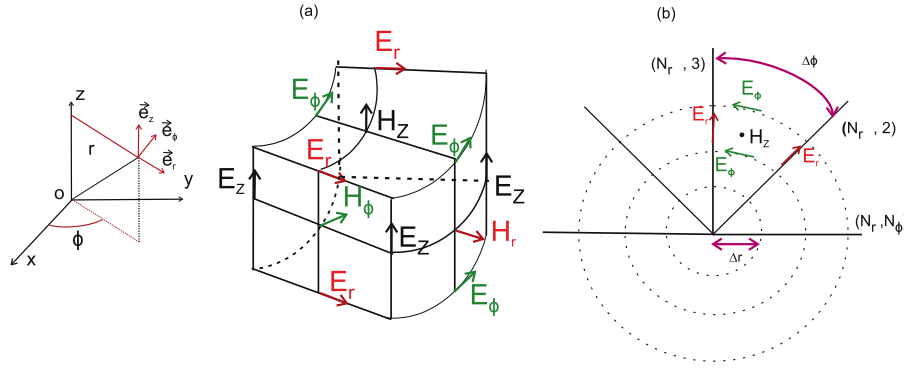   *E-mail address:* fbaida@univ-fcomte.fr (F.I. Baida).

Fig. 1. Positions of the electric and magnetic field components according to the cylindrical Yee scheme in a) 3D case and b) 2D case.

code to the modal study of a metallic CSWG for nano-optical applications.

2. Theoretical developments

The CC-FDTD method is based on the numerical resolution of Maxwell's equations expressed in cylindrical coordinates (system of Eq. (1)) by following the adapted Yee scheme [1,3], shown on Fig. 1.

The CC-FDTD method is based on the numerical resolution of Maxwell's equations expressed in cylindrical coordinates:

$$\frac{\partial D_r}{\partial t} = \frac{1}{r}\frac{\partial H_z}{\partial \phi} - \frac{\partial H_\phi}{\partial z} \tag{1.a}$$

$$\frac{\partial D_\phi}{\partial t} = \frac{\partial H_r}{\partial z} - \frac{\partial H_z}{\partial r} \tag{1.b}$$

$$\frac{\partial D_z}{\partial t} = \frac{1}{r}\left(\frac{\partial (rH_\phi)}{\partial r} - \frac{\partial H_r}{\partial \phi}\right) \tag{1.c}$$

$$-\frac{\partial B_r}{\partial t} = \frac{1}{r}\frac{\partial E_z}{\partial \phi} - \frac{\partial E_\phi}{\partial z} \tag{1.d}$$

$$-\frac{\partial B_\phi}{\partial t} = \frac{\partial E_r}{\partial z} - \frac{\partial E_z}{\partial r} \tag{1.e}$$

$$-\frac{\partial B_z}{\partial t} = \frac{1}{r}\left(\frac{\partial (rE_\phi)}{\partial r} - \frac{\partial E_r}{\partial \phi}\right) \tag{1.f}$$

$\overline{D}$ and $\overline{B}$ are respectively the electric displacement and the magnetic fields. To determine the electromagnetic field $(\overline{E}, \overline{H})$ constitutive relations are needed. In the case of linear, isotropic, homogeneous and non-magnetic medium, these relations can be expressed as:

$$\overline{D}(\omega) = \varepsilon_0 \varepsilon_r(\omega)\overline{E}(\omega) \tag{2.a}$$

$$\overline{B}(\omega) = \mu_0 \overline{H}(\omega) \tag{2.b}$$

Where ω is the angular frequency of the electromagnetic field, ε_0 is the dielectric permittivity of vacuum and $\varepsilon_r(\omega)$ is the dielectric function of the considered medium. μ_0 is the magnetic permeability of vacuum ($\mu_0 \varepsilon_0 c^2 = 1$, with c is the light celerity).

In the scope of the paper, we are only dealing with the determination of the eigenmode properties of an infinite waveguide along the Oz direction.

$$\overline{\psi}(r,\phi,z,t) = \overline{\psi_0}(r,\phi,t)\exp(ik_z z) \tag{3}$$

where $\overline{\psi}$ is any electromagnetic field $(\overline{E}, \overline{D}, \overline{H}, \overline{B})$.

In this case, all the $z-$derivatives of Eq. (1) can be calculated analytically as a function of the wavevector component along the propagation direction through $\frac{\partial \overline{\psi}(r,\phi,z,t)}{\partial z} = ik_z\overline{\psi}(r,\phi,z,t)$ while $r-$, $\phi-$, and $t-$ derivatives are approximated by centered finite differences as in the classical

case of Cartesian coordinates. The r coordinate is discretized as $i\Delta r$, the ϕ one by $j\Delta\phi$ and time by $n\Delta t$ with i, j, n are natural integers and Δr, $\Delta\phi$ and Δt are the step size along each variable. By using the electric constitutive relation Eq. (2.a) and applying the spatial and temporal discretizations, the system of Eq. (1) leads to express the $\overline{D}$ components as:

$$D_r^{n+1}(i,j)$$

$$= D_r^n(i,j) + \triangle t\left[\frac{1}{\left(i+\frac{1}{2}\right)\Delta r}\frac{H_z^{n+\frac{1}{2}}(i,j) - H_z^{n+\frac{1}{2}}(i,j-1)}{\Delta\phi} - ik_z H_\phi^{n+\frac{1}{2}}(i,j)\right] \tag{4.a}$$

$$D_\phi^{n+1}(i,j) = D_\phi^n(i,j) + \triangle t\left[ik_z H_r^{n+\frac{1}{2}}(i,j) - \frac{H_z^{n+\frac{1}{2}}(i,j) - H_z^{n+\frac{1}{2}}(i-1,j)}{\Delta r}\right] \tag{4.b}$$

$$D_z^{n+1}(i,j) = D_z^n(i,j) + \frac{\triangle t}{(i-1)\Delta r}$$
$$\times\left[\frac{\left((i)\Delta r H_\phi^{n+\frac{1}{2}}(i,j) - ((i-1)\Delta r)H_\phi^{n+\frac{1}{2}}(i-1,j)\right)}{\Delta r}\right.$$
$$\left. -\frac{H_r^{n+\frac{1}{2}}(i,j) - H_r^{n+\frac{1}{2}}(i-1,j)}{\Delta\phi}\right] \tag{4.c}$$

The magnetic field components can be obtained similarly.

These equations remain valid for dispersive or non-dispersive dielectric materials. In this last case, the electric field $\overline{E}$ can be instantaneously calculated by dividing the $\overline{D}$ field by $\varepsilon_0\varepsilon_r$.

The stability condition of the CC-FDTD algorithm is given by the Courant-Friedrich-Levy (CFL) criterion [6] as follows:

$$\Delta t = \frac{\alpha}{c}\left(\left(\frac{1}{\triangle r}\right)^2 + \left(\frac{2}{\triangle r \triangle\phi}\right)^2 + \left(\frac{k_z}{2}\right)^2\right)^{-1/2} \tag{5}$$

where α is a less-dimensional coefficient $\in [0,1]$. To avoid the numerical dispersion, the discretization step along the radial direction must verify this condition:

$$\Delta r \leq \frac{\lambda_{min}}{n} \tag{6}$$

where λ_{min} is the minimum wavelength that propagates in the CC-FDTD grid and n is in the range of 15 to 20.

Table 1
Optimized parameters DCP model for Silver in the optical range [400–2500]nm.

	Ag
ε_∞	1.558208
$\omega_D (rad.s^{-1})$	1.387×10^{16}
$\gamma_D (rad.s^{-1})$	3.123×10^{13}
A_1	0.8264434
$\Omega_1 (rad.s^{-1})$	6.792×10^{15}
$\phi_1 (rad)$	−0.785
$\Gamma_1 (rad.s^{-1})$	5.169×10^{15}
A_2	0.3388017
$\Omega_2 (rad.s^{-1})$	6.484×10^{15}
$\phi_2 (rad)$	−0.785
$\Gamma_2 (rad.s^{-1})$	5.402×10^{14}

As we will deal with metallic nano-waveguides in the visible domain, noble metals become dispersive materials. Their dielectric permittivities depend on the frequency. To be implemented in the CC-FDTD algorithm, the constitutive equation linking $\vec{E}$ to $\vec{D}$ must be Fourier transformed as to express the two fields in the time domain. This leads to the calculation of a convolution product that is numerically very difficult to be done. To overcome this constraint, analytical expression of $\varepsilon_r(\omega)$ is needed. Several models where already used and implemented in the FDTD algorithm: simple Drude model [4,14,15], Drude-Lorentz model [16,17], and more recently, the Drude Critical Points (DCP) model [9–11]. This later is considered as the more accurate model to faithfully describe the dielectric properties of noble metals in the visible to near infrared domain.

The frequency dependence of the dielectric permittivity for the DCP model with only two terms (this is enough in the case of silver for example) is given by:

$$\varepsilon_r(\omega) = \varepsilon_{DCP}(\omega) = \varepsilon_\infty - \frac{\omega_D^2}{\omega^2 + i\gamma_D\omega} + \sum_{p=1}^{p=2} G_p(\omega) \tag{7}$$

where:

$$G_p(\omega) = A_p\Omega_p \left(\frac{\exp(i\phi_p)}{\Omega_p - \omega - i\Gamma_p} + \frac{\exp(-i\phi_p)}{\Omega_p + \omega + i\Gamma_p} \right)$$

The first two terms of Eq. (7) correspond to the classical Drude contribution (ε_∞ is the dielectric function at high frequency, ω_D is the plasma frequency of the metal, γ_D is the damping term). The third term which is a sum over the integer p represents the contribution of inter-band transitions, with amplitude A_p, energy gap Ω_p, phase ϕ_p and damping factor Γ_p [18,19]. To our knowledge, this is the first time that this model is implemented in the CC-FDTD algorithm. For this purpose, and for the sake of simplicity, the displacement vector $\vec{D}$ is written as

the sum of three terms, each one corresponding to one contribution to the dielectric function of Eq. (7):

$$\overline{D}(\omega) = \overline{D}_D(\omega) + \overline{D}_{C1}(\omega) + \overline{D}_{C2}(\omega) \tag{8}$$

where:

$$\overline{D}_D(\omega) = \varepsilon_0 \left[\varepsilon_\infty - \frac{\omega_D^2}{\omega^2 + i\gamma_D\omega} \right] \vec{E}(\omega) \tag{9.a}$$

$$\overline{D}_{Cp}(\omega) = \varepsilon_0 \left[A_p\Omega_p \left(\frac{\exp(i\phi_p)}{\Omega_p - \omega - i\Gamma_p} + \frac{\exp(-i\phi_p)}{\Omega_p + \omega + i\Gamma_p} \right) \right] \vec{E}(\omega) \quad p = 1, 2 \tag{9.b}$$

As mentioned before, the implementation of Eq. (9.a) and Eq. (9.b) into the CC-FDTD algorithm requires to calculate their inverse Fourier transformations in order to express the fields in the temporal domain:

$$\left(\frac{\partial^2}{\partial t^2} + \gamma \frac{\partial}{\partial t} \right) \overline{D}_D(t) = \varepsilon_0 \varepsilon_\infty \left(\frac{\partial^2}{\partial t^2} + \gamma_D \frac{\partial}{\partial t} + \frac{\omega_D^2}{\varepsilon_\infty} \right) \vec{E}(t) \tag{10.a}$$

$$\left(\Omega_p^2 + \Gamma_p^2 + \frac{\partial^2}{\partial t^2} + 2\Gamma_p \frac{\partial}{\partial t} \right) \overline{D}_{Cp}(t)$$
$$= 2\varepsilon_0 A_p\Omega_p \left(\sqrt{\Gamma_p^2 + \Omega_p^2} \sin(\theta_p - \phi_p) - \right.$$
$$\left. - \sin\phi_p \frac{\partial}{\partial t} \right) \vec{E}(t) \tag{10.b}$$

where: $\theta_p = \arctan(\frac{\Omega_p}{\Gamma_p})$

After discretization of Eq. (10.a) and Eq. (10.b) through centered finite differences scheme we obtain the relationship that gives the electric field components as a function of the displacement field ones. An example is given by Eq. (11) for the electric r component:

$$E_r^{n+1} = \frac{1}{\frac{\chi_D}{\alpha_D} + \sum_{p=1}^{p=2} \left(\frac{\chi_p}{\alpha_p} \right)}$$
$$\times \left[D_r^{n+1} + \frac{\beta_D}{\alpha_D} D_{D_r}^{n-1} + \frac{4}{\alpha_D} D_{D_r}^n - \frac{\delta_D}{\alpha_D} E_r^{n-1} - \frac{4\varepsilon_0\varepsilon_\infty}{\alpha_D} E_r^n \right.$$
$$\left. + \sum_{p=1}^{p=2} \left(\frac{\beta_p}{\alpha_p} D_{Cp_r}^{n-1} - \frac{4}{\alpha_p} D_{Cp_r}^n \right) + \sum_{p=1}^{p=2} \left(\frac{\delta_p}{\alpha_p} \right) E_r^{n-1} \right] \tag{11}$$

The values of α_D, β_D, χ_D, δ_D, α_D, β_p, χ_p and δ_p are given in Table 1, which are optimized according to the experimental data of ref. [20].

3. Validation and convergence tests

The CC-FDTD code implemented as part of this work has been the subject of many validation tests. The first tests were performed in the

(a)   (b)

Coax waveguide (CWG)   **C-shaped waveguide (CSWG)**
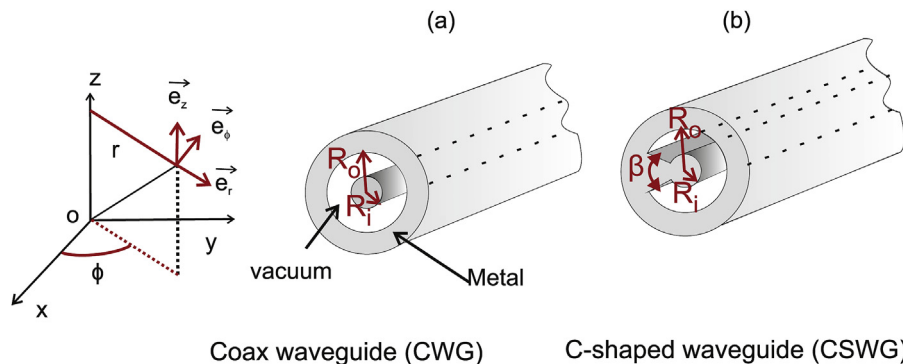
Fig. 2. Schematic of the studied metallic waveguides where R_i is the inner radius and R_o is the outer radius of (a) the coax waveguide (CWG) and (b) the C-shaped waveguide (CSWG). In (b), β is the angle delimiting the additional metallic part of the CSWG.
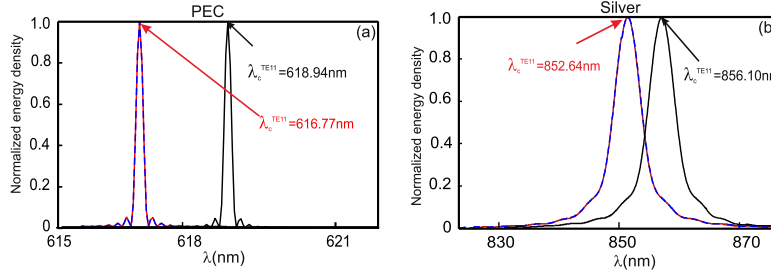
Fig. 3. Normalized energy density at the cutoff ($k_z = 0$) of CWG with $R_i = 74$ nm and $R_o = 124$ nm. a) Perfect conducting metal (PEC) and b) Silver (real metal). The red curves correspond to the CC-FDTD calculations, the dashed blue curves correspond to the BOR-FDTD calculations and the black curves correspond to the FDTD calculations. (For interpretation of the references to colour in this figure legend, the reader is referred to the Web version of this article.)

case of a waveguide having a symmetry of revolution. For this, we consider the coaxial waveguide (CWG) studied in Ref. [4] (see Fig. 2.a). The spectral energy densities for $k_z = 0$, calculated by the CC-FDTD code, the BOR-FDTD code used in that reference [4] and by a conventional FDTD code (in Cartesian coordinates) are shown on Fig. 3. The case of a perfect conducting metal (PEC) and silver (Ag) are presented on Fig. 3.a and b respectively where the inner and outer radii are fixed to $R_i = 74$ nm and $R_o = 124$ nm. The discretization of the radial coordinate is fixed to $\Delta r = 0.5$ nm in both CC-FDTD and BOR-FDTD codes while $\Delta\phi = 1^o$ in the CC-FDTD and $\Delta x = \Delta y = 0.5$ nm in the FDTD code. However, for the perfect conductor case, the cutoff wavelength λ_c of the TE_{11} mode is given by the equation [21]:

$$J_1'\left(\frac{2\pi}{\lambda_c}R_i\right)Y_1'\left(\frac{2\pi}{\lambda_c}R_o\right) - J_1'\left(\frac{2\pi}{\lambda_c}R_o\right)Y_1'\left(\frac{2\pi}{\lambda_c}R_i\right) = 0 \qquad (12)$$

where J_1' and Y_1' are the derivatives of the Bessel functions of the first and second kinds respectively.

The numerical solution of this equation leads to $\lambda_c^{ana} = 615.97$ nm which is slightly different from the approximated value $\lambda_c^{app} = \pi(R_o + R_i) = 622.03$ nm. Contrariwise, the value calculated by both CC-FDTD and BOR-FDTD ($\lambda_c^{CC-FDTD} = \lambda_c^{BOR-FDTD} = 616.77$ nm) is more accurate (see Fig. 3.a). The results show a perfect agreement between the CC-FDTD and BOR-FDTD codes and give the same value of the cutoff wavelength for the fundamental guided mode (TE_{11}). However, the FDTD simulations lead to a larger value $\lambda_c^{FDTD} = 618.94$ nm for the same mesh size.

Thereby, we have performed convergence test in order to determine the accuracy of the CC-FDTD simulations in comparison with the conventional FDTD. For this purpose, we consider the same CWG and we determine λ_c by varying both Δr and $\Delta\phi$ in the CC-FDTD code while only $\delta = \Delta x = \Delta y$ is varied in the FDTD simulations. Fig. 4.a shows the results of the FDTD simulations when $\delta = [0.1, 0.2, 0.4, 0.5, 1, 2]$ nm. All these values are divisors of both R_i and R_o as to get a better description of the structure (integer number of cells). The same calculation is re-done via the CC-FDTD code by varying $\Delta r = [0.1, 0.2, 0.4, 0.5, 1, 2]$ nm and $\Delta\phi = [1, 4, 8, 12, 18, 30, 36](^o)$. To numerically recover the analytical value of the cutoff wavelength, we assume a maximum relative error of $\frac{\Delta\lambda}{\lambda_c^{ana}} = 0.5\%$. Thus, for $\lambda_c^{ana} = 615.97$ nm we get $\triangle\lambda = 3$ nm. Green dashed areas on Fig. 4.a–c correspond to this condition. For the FDTD (see Fig. 4.a), a fine mesh of $\delta_{max} \leq 0.5$ nm is required. Concerning the CC-FDTD, if a small radial step size (Δr) is considered, a coarse angular discretization ($\Delta\phi$) is allowed and *vice versa*. For example, a $\Delta r = 0.4$ nm requires a $\triangle\phi$ of only 18° (see point A on Fig. 4.b) while a value of $\Delta r = 1$ nm imposes a maximum $\Delta\phi$ of 12° (see point B on Fig. 4.c). Nevertheless, for $\Delta\phi > 24^o$ a very fine radial mesh ($\Delta r < 0.1$ nm) is required leading to a huge numerical simulation. Finally, for the same CWG structure, an accurate simulation by FDTD of a 300×300 nm^2 window requires a discretization with 360000 cells ($\delta = 0.5$ nm) while a CC-FDTD code needs 7500 cells ($\Delta r = 0.4$ nm and $\Delta\phi = 18^o$). Consequently, the CC-FDTD code allows us to gain both memory (1:48) and CPU time (1:12).
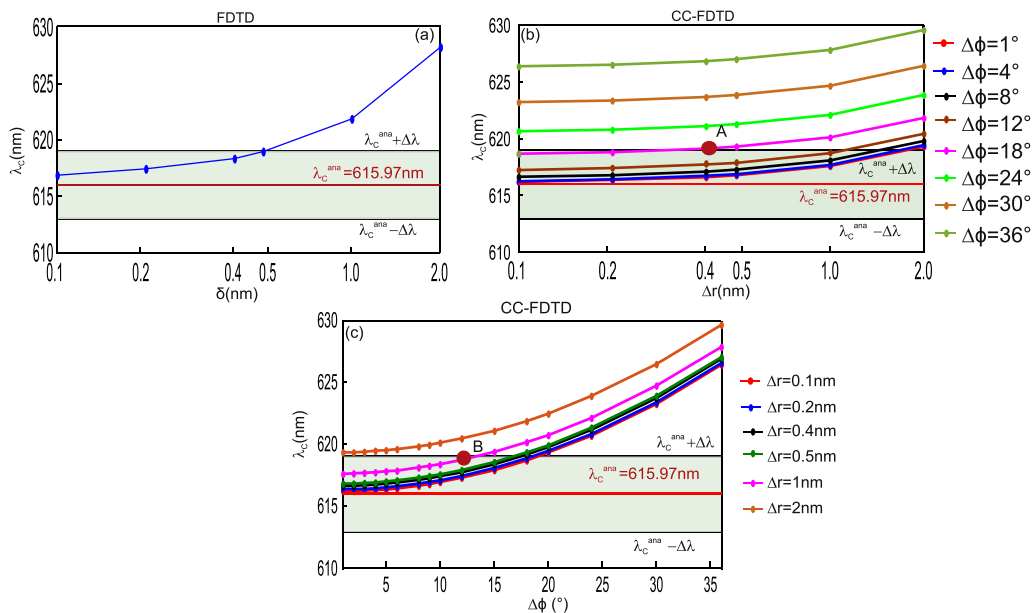
Fig. 4. Convergence tests for conventional FDTD and CC-FDTD: Calculation of the fundamental mode cutoff wavelength versus the discretization steps for the PEC-CWG with: $R_i = 74$ nm and $R_o = 124$ nm.

4. Application: study of a C-shaped waveguide

To take advantage from the developed CC-FDTD code, we perform here a systematic study of a C-shaped waveguide. Let us first recall the main improvement that is provided by this structure with respect to a coaxial waveguide [4] in the context of enhanced transmission metamaterials. In fact, the main discrepancy is due to the cutoff of the fundamental guided mode of each structure. For the CWG, an approximated value of the cutoff wavelength of this mode (TE_{11}) is given by $\lambda_c^{TE11} \simeq \pi(R_i + R_o)$ which corresponds to the average length of coaxial section (perimeter of the medium circle). In the case of the CSWG, and assuming R_o tends to R_i, the waveguide behaves as a curved rectangular one with a TE_{10} fundamental mode exhibiting a cutoff of $\lambda_c^{TE10} = 2 \times L$ where L is the average length of the section. According to notations of Fig. 2.b, this length is given by $L = (\pi - \beta/2)(R_o + R_i)$. Thus, this cutoff ($TE_{10}$ mode) can be two times greater than the one of the TE_{11} mode of the CWG when $\beta \to 0$. Consequently, for the same radii, the CSWG admits a TE_{10} mode that can be excited at wavelengths greater than the TE_{11} mode of a coaxial waveguide as long as $\beta < \pi$.

An example is given on Fig. 5 where radii are the same for the CWG and the CSWG ($R_i = 74$ nm and $R_o = 124$ nm) and β is fixed to 30° for the CSWG. One can see that, in the case of a PEC, the cutoff wavelength of the TE_{10} mode is $\lambda_c^{TE10} = 1139.24$ nm for the CSWG while the cutoff wavelength of the TE_{11} mode of the CWG is only $\lambda_c^{TE11} = 616.77$ nm (see dashed curves of Fig. 5: red for CWG and blue for the CSWG). Similar simulations were done in the case of silver (see solid lines of Fig. 5: red for CWG and blue for the CSWG). In this case, the cutoff wavelengths are $\lambda_c^{TE11} = 852.64$ nm and $\lambda_c^{TE10} = 1656.85$ nm for the CWG and the CSWG respectively. The maps of the electric field intensity of these two guided modes are given on the right of Fig. 5 in a logarithmic scale to point out the penetration of the electric field inside the metal. In both cases, the numerical simulations are performed with small values of $\Delta r = 0.5$ nm and $\Delta \phi = 1^o$ in order to get a high image resolution. These simulations were performed over a total real time (time of light-matter interaction) of $t = 1.56 \times 10^3 fs$ with a time step of $\Delta t = 1.85 \times 10^{-5} fs$. One can notice that the redshift of the fundamental mode cutoff when passing from the CWG to the CSWG becomes larger in the case of metal with dispersion (silver for instance). Thus, if we define $\delta \lambda = \lambda_c^{TE10} - \lambda_c^{TE11}$, we get $\delta \lambda^{PEC} \simeq 552$ nm $< \delta \lambda^{Ag} \simeq 805$ nm. This confirms the interesting properties of the CSWG and justify our present study.

In addition to its compactness, this structure provides a breaking symmetry and therefore it is promising for the realization of metama-

Fig. 6. Dispersion curves of a silver CSWG with three values of R_e with $R_i = 74$ nm and $\beta = 30^o$.

terials exhibiting original properties such as negative refractive index [22–24] or artificial anisotropy [25,26] with extraordinary birefringence ($\Delta n \sim 0.75$ [27]).

Due to these interesting properties, structures based on array of C-shaped apertures [28], single C-shaped straight or bent waveguides [29,30] were studied both theoretically [29,30] and experimentally [31,32]. Nevertheless, in all these studies, the C-shape is obtained with three straight line segments and it presents two corners with 90° angle. Unfortunately, the fabrication of such structure is a very difficult task especially if we design it to operate in the optical domain where dimensions become very small ($R_i < R_o < 200$ nm). Thus, it is more accurate to consider smooth-edge structures such as curved C-shaped ones as depicted on Fig. 2.b.

In order to point out the propagation properties in the case of CSWG made in silver, we calculated the dispersion curve $\omega = f(k_z)$ (see Fig. 6) for different values of the outer radius (R_o) and an inner radius fixed to $R_i = 74$ nm. The obtained dispersion curves cut the light line confirming an hybrid character of the fundamental mode (propagative-plasmonic). In addition, we have verified that when $R_o \to R_i$ the cutoff frequency tends to zero ($\lambda_c \to \infty$). This behavior has already been observed by Baida et al. in Ref. [4] (see Fig. 3 of that reference) in the case of a coaxial waveguide made in silver and by Lindfors et al. in Ref. [33] in the case of a rectangular waveguide made in gold. The origin of this unexpected behavior is attributed by the authors to the plasmonic characters of this mode [4,33].

Fig. 7 shows the energy distribution of the fundamental mode at the cutoff wavelength ($k_z = 0$) calculated for different values of the outer radius. These images show that the light intensity corresponds to the excitation of the inner interface surface plasmon mode of the CSWG. For R_o value close to the R_i one, the maximum intensity of the mode
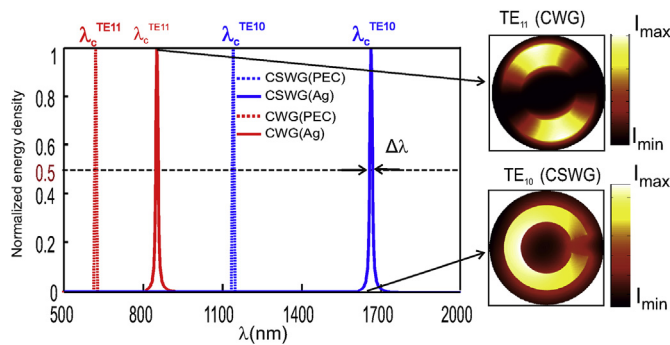

Fig. 5. In-plane modes ($k_z = 0$) normalized energy densities for ($k_r = k_\phi = 0$) of both CWG (red curves) and CSWG (blue curves) with $\beta = 30^o$, $R_i = 74$ nm and $R_o = 124$ nm. The dashed lines correspond to the case of PEC while the solid lines refer to the case of silver. Note that only the first guided mode with cutoff of each structure is presented. The right column shows the electric intensity distributions (in logarithmic scale) at the cutoff wavelength of each structure made in silver. (For interpretation of the references to colour in this figure legend, the reader is referred to the Web version of this article.)
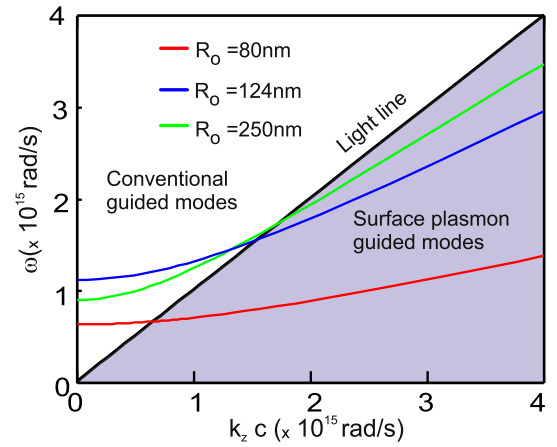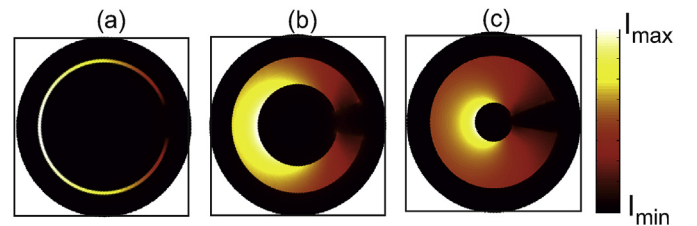

Fig. 7. Electric intensity distributions of the fundamental mode TE_{10} at cutoff wavelength for silver CSWG with $R_i = 74$ nm and $\beta = 30^o$. a) $R_o = 80$ nm, b) $R_o = 124$ nm and c) $R_o = 250$ nm.

TE_{10} reaches the opposite second interface (outer metallic part). Thus, a coupling between the two interfaces appears leading to an effective mode that penetrates more importantly inside the metallic parts of the waveguide. Obviously, this leads to increase the losses.

For applications in nano-optics, it is essential to quantify optical losses as a function of the wavelength. For this purpose, we calculate the real and imaginary part of the effective index of the TE_{10} mode as a function of the wavelength for three different values of the outer radii. The real part of the effective index is given by the relation $n'_{eff} = \frac{k_z c}{\omega}$ and can be directly obtained from the dispersion curve of Fig. 6. As expected, the values of n'_{eff} (see Fig. 8.b) are greater than the ones of the coaxial waveguide [4] due to the fact that the cutoff wavelength is redshifted. The determination of the imaginary part of the effective index n''_{eff} is realized after estimating the *FWHM* (Full Width at Half Maximum) $\Delta\lambda$ of the spectral density peak (see Fig. 5) through the relation:

$$n''_{eff} = \frac{\Delta\lambda}{\lambda} \tag{13}$$

From the n''_{eff} values obtained, we estimated the propagation distances using the following formula:

$$L_P = \frac{\lambda}{2\pi n''_{eff}} \tag{14}$$

Fig. 8.c shows the variation of the imaginary part of the effective index as a function of the wavelength for three different CSWG outer radii: $R_o = 80$ nm, 124 nm, 250 nm when R_i is fixed to 74 nm. The variations of the propagation distance for the same three values of R_o are given on Fig. 8.d. One notes that the propagation distances increase with R_o i.e. when the inter-conductor space expands. We can interpret this phenomenon from the light intensity distributions that inform us about the light penetration inside the metal (see Fig. 5).

For large value of R_o, the guided energy is almost located inside the inner-conductor area (vacuum) and it extends over the metal when R_o decreases. This interpretation is confirmed by the dispersion curves that show low curve slope ω function of k_z (low group velocity) when the inter-conductor space is small. These propagation distances estimated
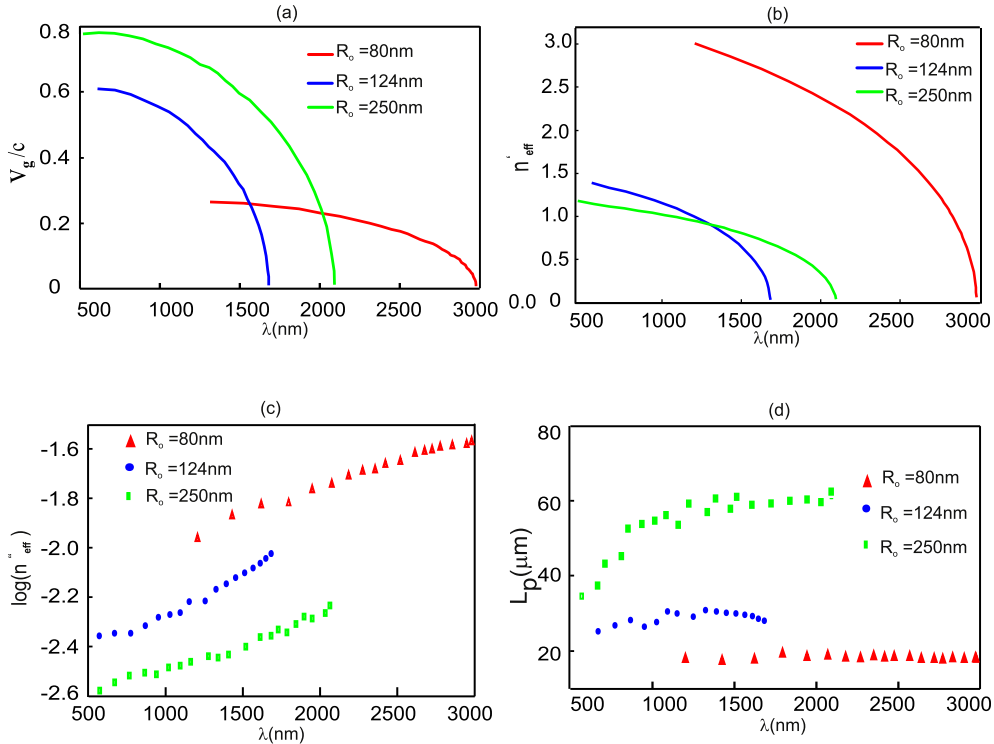
Fig. 8. a) Normalized group velocity (by c) for silver CSWG with $R_i = 74$ nm, $R_o = 124$ nm and $\beta = 30^o$, b) Real part and c) imaginary part of the effective index for the fundamental mode TE_{10}. d) Propagation length (L_P) corresponding to the same mode.
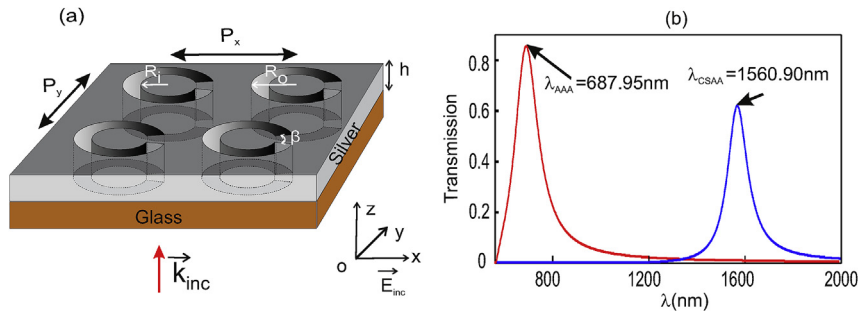
Fig. 9. a) Schematic of the CSAA structure illuminated under normal incidence by a plane wave linearly polarized along the x-direction. The geometrical parameters are $R_i = 50$ nm, $R_o = 100$ nm, $h = 100$ nm and $P_x = P_y = 350$ nm. b) Transmission spectra through the CSAA structure (in blue with $\beta = 30^o$) compared to the case of the AAA structure with the same geometrical parameters (in red with $\beta = 0^o$). (For interpretation of the references to colour in this figure legend, the reader is referred to the Web version of this article.)

to $L_P = 60 \, \mu m$ (case of $R_i = 74$ nm and $R_o = 250$ nm) which is large enough for applications in nano-optics.

The variation of the fundamental mode group velocity deduced from the dispersion curves ($v_g = \frac{d\omega}{dk}$), for $R_i = 74$ nm and $R_o = 124$ nm is shown in Fig. 8.a. Note that this velocity is very small compared to the velocity of light in vacuum and in particular when λ tends to λ_c. That slow light can be exploited to exalt nonlinear effects by filling the inter conductor space with a nonlinear material such as in Ref. [34].

To emphasize the properties of the C-shaped structure, we propose to use it as an enhanced transmission metamaterial instead of an AAA (Annular Aperture Array) that was theoretically [35] and experimentally studied [36] to demonstrate enhanced transmission up to 92% in the visible range. For this purpose, we consider an array of C-shaped apertures engraved on a metal film of thickness h and deposited on a glass substrate ($n = 1.5$) as presented on Fig. 9.a. The period P of the array is chosen so that, the cutoff wavelength of the fundamental mode is larger than the Rayleigh anomaly wavelength give by $\lambda_R = n \times P$. Fig. 9.b shows the simulated transmission spectra for both the AAA [12] and CSAA (C-Shaped Aperture Array) structures. As expected, transmission peaks ($T_{AAA} = 85\%$ at $\lambda_{AAA} = 687.94$ nm and $T_{CSAA} = 62\%$ at $\lambda_{CSAA} = 1568.90$ nm) appear at a wavelength closer to the guided mode cutoff one in both cases. Consequently, the C-shaped structure appears to be more adequate in the context of enhanced transmission due to the fact that it can handle guided modes with large value of wavelength compared to the coaxial structure. This opens new perspectives in the miniaturization of components for enhanced transmission applications, such as artificial birefringent metamaterials [25,27].

5. Conclusion

The CC-FDTD algorithm developed in this work allows us a better description of the curved geometry of any structure exhibiting total or partial cylindrical symmetry. Many validation and convergence tests are performed in comparison with FDTD and BOR-FDTD algorithms. The obtained results, that show a very good agreement, validate our approach and demonstrate a gain in both memory space and CPU time calculation. The developed code was subsequently used to realize a parametric study of a CSWG made in silver. This waveguide can handle largest beam wavelengths compared to waveguides with other geometric shapes. The CSWG allows for propagation of the optical signal over quite long distances of the order of several tens of micrometers without much attenuation via its fundamental mode (TE_{10}). The group velocity associated with this fundamental mode is low allowing enhancement of nonlinear effects [34,37]. All these optical properties show that CSWG is a very good candidate for applications in nano-optics.

Acknowledgments

Appendix A. Supplementary data

Supplementary data related to this article can be found at https://doi.org/10.1016/j.physb.2017.12.054.

References

[1] A. Taflove, S. Hagness, Computational Electromagnetics: the Finite-difference Time-domain Method, Artech House, Boston, 2000.
[2] F. Baida, A. Belkhir (Eds.), Finite Difference Time Domain Method for Grating Structures, AMU (PUP), 2012, pp. 1–9.
[3] K.S. Yee, Numerical solution of initial boundary value problems involving Maxwell's equations in isotropic media, IEEE Trans. Antenn. Propag. 14 (1966) 302–307.
[4] F.I. Baida, A. Belkhir, D. Van Labeke, O. Lamrous, Subwavelength metallic coaxial waveguides in the optical range: Role of the plasmonic modes, Phys. Rev. B. 74 (2006) 205419.
[5] Y. Chen, R. Mittra, P. Harms, Finite-difference time-domain algorithm for solving Maxwell's equations in rotationally symmetric geometries, IEEE Trans. Microw. Theor. Tech. 44 (1996) 832–839.
[6] N. Dib, T. Weller, M. Scardelletti, M. Imparato, Analysis of cylindrical transmission lines with the finite-difference time-domain method, IEEE Trans. Microw. Theor. Tech. 47 (1999) 509–512.
[7] Tomasz J. Antosiewicz, P. Wróbel, T. Szoplik, Magnetic field concentrator for probing optical magnetic metamaterials, Opt. Exp. 25 (2010) 25906–25911.
[8] P. Wróbel, Piotr, Tomasz J. Antosiewicz, T. Szoplik, Plasmonic concentrator of magnetic field of light, J. Appl. Phys. 112 (2012) 074304.
[9] A. Vial, Implementation of the critical points model in the recursive convolution method for modelling dispersive media with the finite-difference time domain method, J. Opt. A: Pure Appl. Opt. 9 (2007) 745–748.
[10] A. Vial, T. Laroche, Comparison of gold and silver dispersion laws suitable for FDTD simulations, Appl. Phys. B 93 (2008) 139–143.
[11] M. Hamidi, F.I. Baida, A. Belkhir, O. Lamrous, Implementation of the critical points model in a SFM-FDTD code working in oblique incidence, J. Phys. D: Appl. Phys. 44 (2011) 245101.
[12] F.I. Baida, D. Van Labeke, G. Granet, A. Moreau, A. Belkhir, Origin of the super-enhanced light transmission through a 2-D metallic annular aperture array: a study of photonic bands, Appl. Phys. Lett. 79 (2004) 1–8.
[13] C.T. Chan, Q.L. Yu, K.M. Ho, Order-N spectral method for electromagnetic waves, Phys. Rev. B 51 (1995) 16635.
[14] M. Hamidi, C. Chemrouk, A. Belkhir, Z. Kebci, A. Ndao, O. Lamrous, F. Baida, SFM-FDTD analysis of triangular-lattice AAA structure: Parametric study of the TEM mode, Opt. Commun. 318 (2014) 47–52.
[15] R.M. Joseph, S.C. Hagness, A. Taflove, Direct time integration of Maxwell's equations in linear dispersive media with absorption for scattering and propagation of femtosecond electromagnetic pulses, Opt. Lett. 16 (1991) 1412–1414.
[16] A.A. Vial, A.-S. Grimault, D. Macías, D. Barchiesi, M.L. de La Chapelle, Improved analytical fit of gold dispersion: Application to the modeling of extinction spectra with a finite-difference time-domain method, Phys. Rev. B 71 (2005) 085416.
[17] F. Baida, A. Belkhir, Superfocusing and light confinement by surface plasmon excitation through radially polarized beam, Plasmonics 4 (2009) 51–59.
[18] P.G. Etchegoin, E.C.L. Ru, M. Meyer, An analytic model for the optical properties of gold, J. Chem. Phys. 125 (2006) 164705.
[19] P.G. Etchegoin, E.C.L. Ru, M. Meyer, Erratum: An analytic model for the optical properties of gold, J. Chem. Phys. 127 (2007) 189901.
[20] E. Palik, Handbook of Optical Constants of Solids, Academic Press, 1998.
[21] J.D. Jackson, C. Jeanmougin, J.-P. Vigneron, Classical electrodynamics: Courses and exercises of electromagnetism, Dunod, 2001.
[22] J.B. Pendry, A.J. Holden, D. Robbins, W. Stewart, Magnetism from conductors and enhanced nonlinear phenomena, IEEE Trans. Microw. Theor. Tech. 47 (1999) 2075–2084.
[23] D.R. Smith, W.J. Padilla, D. Vier, S.C. Nemat-Nasser, S. Schultz, Composite medium with simultaneously negative permeability and permittivity, Phys. Rev. Lett. 84 (2000) 4184.
[24] A.O. Cakmak, K. Aydin, E. Colak, Z. Li, F. Bilotti, L. Vegni, E. Ozbay, Enhanced transmission through a subwavelength aperture using metamaterials, Appl. Phys. Lett. 95 (2009) 052103.
[25] F. Baida, M. Boutria, R. Oussaid, D. Van Labeke, Enhanced-transmission metamaterials as anisotropic plates, Phys. Rev. B. 84 (2011) 035107.
[26] M. Boutria, R. Oussaid, D. Van Labeke, F.I. Baida, Tunable artificial chirality with extraordinary transmission metamaterials, Phys. Rev. B. 86 (2012) 155428.
[27] J. Dahdah, J. Hoblos, F.I. Baida, Nanocoaxial waveguide grating as quarter-wave plates in the visible range, IEEE Photon. J 4 (2012) 87–94.
[28] J. Lee, M. Seo, D. Park, D. Kim, S. Jeoung, C. Lienau, Q.-H. Park, P. Planken, Shape resonance omni-directional terahertz filters with near-unity transmittance, Opt. Exp. 14 (2006) 1253–1259.
[29] L. Sun, L. Hesselink, Low-loss subwavelength metal C-aperture waveguide, Opt. Lett. 31 (2006) 3606–3608.
[30] P. Hansen, L. Hesselink, B. Leen, Design of a subwavelength bent C-aperture waveguide, Opt. Lett. 32 (2007) 1737–1739.
[31] X. Shi, L. Hesselink, R.L. Thornton, Ultrahigh light transmission through a C-shaped nanoaperture, Opt. Lett. 28 (2003) 1320–1322.
[32] J.W. Lee, M. Seo, D. Kim, J. Kang, Polarization dependent transmission through asymmetric C-shaped holes, Appl. Phys. Lett. 94 (2009) 081102.
[33] K. Lindfors, L. Lechner, M. Kaivola, Dependence of resonant light transmission properties of a subwavelength slit on structural parameters, Opt. Exp. 17 (2009) 11026–11038.
[34] E. Barakat, M.-P. Bernal, F.I. Baida, Theoretical analysis of enhanced nonlinear conversion from metallo-dielectric nano-structures, Opt. Lett. 20 (2012) 16258–16268.
[35] F.I. Baida, D. Van Labeke, Three-dimensional structures for enhanced transmission through a metallic film: Annular aperture arrays, Phys. Rev. B 67 (2003) 155314.
[36] Y. Poujet, J. Salvi, F.I. Baida, 90% extraordinary optical transmission in the visible range through annular aperture metallic arrays, Opt. Lett. 32 (2007) 2942–2944.
[37] M. Roussey, M.-P. Bernal, N. Courjal, D. Van Labeke, F. Baida, R. Salut, Electro-optic effect exaltation on lithium niobate photonic crystals due to slow photons, Appl. Phys. Lett. 89 (2006) 241110.